Available online at www.sciencedirect.com
SCIENCE DIRECT®
Tectonophysics 377 (2003) 357–381
TECTONOPHYSICS
www.elsevier.com/locate/tecto

Subcritical compaction and yielding of granular quartz sand

Stephen L. Karner*, Frederick M. Chester, Andreas K. Kronenberg, Judith S. Chester

Center for Tectonophysics, Department of Geology and Geophysics, Texas A&M University, College Station, TX 77845, USA

Received 18 February 2003; accepted 15 October 2003

Abstract

Cylindrical samples of water-saturated, initially loose, St. Peter quartz sand were consolidated using triaxial deformation apparatus at room temperature, constant fluid pressure (12.5 MPa), and elevated confining pressures (up to 262.5 MPa). The samples were deformed along four loading paths: (1) hydrostatic stressing tests in which confining pressure was monotonically increased; (2) hydrostatic stress cycling similar to (1) except that effective pressure was periodically decreased to initial conditions; (3) triaxial deformation at constant effective pressure in which differential stress was applied after raising effective pressure to an elevated level; and (4) triaxial stress cycling similar to (3) except that the axial differential stress was periodically decreased to zero. Hydrostatic stressing at a constant rate results in a complex nonlinear consolidation response. At low pressures, large strains occur without significant acoustic emission (AE) activity. With increased pressure, the stress versus strain curve becomes quasi-linear with a corresponding nonlinear increase in AE rates. At elevated pressures, macroscopic yielding is marked by the onset of large strains, high AE rates, and significant grain failure. Stress cycling experiments show that measurable inelastic strain occurs at all stages of hydrostatic loading. The reload portions of stress cycles are characterized by a poro-elastic response and lower AE rates than during constant rate hydrostatic stressing. As the stress nears and exceeds the level that was applied during previous loading cycles, strain and AE rates increase in a manner consistent with yielding. Triaxial stressing cycles achieve greater consolidation and AE rates than hydrostatic loading at similar mean stress levels. By comparing our results with previously published studies, we construct a three-component model to describe elastic and inelastic compaction of granular sand. This model involves acoustically silent grain rearrangement that contributes significant inelastic strain at low pressures, poro-elastic (Hertzian) deformation at all pressures, and inelastic strain related to granular cracking and particle failure which increases in significance at greater pressures.

Keywords: Compaction; Deformation; Flow; Fracture; Sand; Sedimentary

1. Introduction

Understanding the processes associated with consolidation and densification of granular media is fundamental for many research topics in the Earth sciences: such as mass movement (e.g. landslides, turbidity flows), pyroclastic flows, high-velocity planetary impacts, migration of mantle melt, sediment transport, burial diagenesis of sedimentary rocks, and shear-enhanced evolution of fault zone materials (gouge). Loose sediments compact to form consolidated rock when subjected to the physico-chemical conditions associated with burial (e.g. pressure, tem-

* Corresponding author. Fax: +1-979-845-6162.
E-mail address: karner@geo.tamu.edu (S.L. Karner).

0040-1951/$ - see front matter
doi:10.1016/j.tecto.2003.10.006

perature, presence and type of fluids). The path by which sediments become lithified plays a major role in determining the various physical properties of sedimentary rocks (e.g. mineralogy, degree of grain packing, bulk strength, permeability, porosity). Similarly, consolidation processes can significantly alter the strength and flow properties of granular fault gouge. Thus, in order to properly understand the material properties and evolution of these granular systems, it is necessary to first understand how the granular medium responds to deformation.

In material science and soil mechanics, a deforming granular aggregate is often considered to be an elasto-plastic material. This concept has been perpetuated by the continued testing of clay-rich soils sparked by the pioneering work of Terzaghi (1925). That is, stressing of a porous media is considered to induce an initial stage of elastic deformation followed by an interval of non-recoverable strain similar to plastic flow. As such, there are several descriptive statements that are used to define the stress–strain behaviour of the deforming granular medium (Britto and Gunn, 1987): (1) a yield function for the material; (2) an expression relating directions of principal strains to principal stresses; (3) a flow rule; and (4) post-yield deformation style.

The key aspects in this definition are that the material is elasto-plastic and that it exhibits a distinct yield point. By definition, yielding occurs when a material is strained beyond its elastic limit whereby subsequent strain cannot be recovered when the applied stresses are relaxed. Below the elastic limit where the yield condition has not yet been satisfied, a material is considered to be either rigid or in a state of elastic deformation. It is this strict definition of yield that is used to describe the yield function which, in turn, defines the stress–strain characteristics of a deforming media. Compaction experiments on sandstones appear to follow this style of deformation (e.g. Brace, 1978; Zhang et al., 1990a,b). Volumetric strains are nonlinear at low stresses, with a transition to quasi-linear loading as applied stress increases (resembling the behaviour of an elastic material). This quasi-linear loading trend continues to an inflection point (P*) above which volumetric strains accelerate and show measurable permanent deformation (Zhang et al., 1990a,b). This latter stage is associated with large acoustic emission rates (indicative of fracturing processes) and pervasive grain crushing, in a manner consistent with sample yield. In practice, however, materials may not display such idealized yield behaviour.

Studies of deformation in sands (e.g. Zoback and Byerlee, 1976; Brzesowsky, 1995) and sandstones (e.g. Zhang et al., 1990a,b; David et al., 1994; Wong et al., 1997; Baud et al., 2000) show that the critical pressure, P*, marks the onset of pervasive grain crushing. Clearly, grain-scale brittle deformation at P* is associated with macroscopic sample yield and involves permanent damage leading to non-recoverable strains and porosity loss coupled with a reduction in permeability (e.g. Zoback and Byerlee, 1976). However, it is unclear exactly how deformation is accommodated at pressures below the macroscopic crushing strength, P*. Is strain within a deforming granular aggregate accommodated via purely elastic means, or are other inelastic mechanisms involved in deformation?

To investigate deformation at sub-critical pressures and to help isolate relative contributions from elastic and inelastic strain mechanisms, we performed compaction experiments on cohesionless samples of granular quartz sand in standard triaxial deformation apparatus. Our samples exhibit deformation behaviour consistent with results from sandstones (e.g. Zhang et al., 1990a,b), compaction in soils (e.g. Terzaghi, 1925; Britto and Gunn, 1987; Bridgwater, 1994), consolidation of oceanic sediments (e.g. Olgaard et al., 1995), and poro-elastic models of granular deformation (Hertz, 1881; Mindlin and Deresiewicz, 1953; Gangi, 1978; Brzesowsky, 1995). Taken collectively, these studies indicate that granular deformation involves both elastic and inelastic mechanisms that operate simultaneously. Thus, care must be taken to correctly identify the modes of strain accommodation—particularly leading to the functional description of yield.

2. Experiment procedure

2.1. Experiment sample and preparation

St. Peter quartz sand was chosen for this study and was collected from Battle Creek in Minnesota, USA. The St. Peter formation is a very pure, fine-grained, well-sorted, friable quartzose sandstone of middle Ordovician age probably deposited in a near-shore, transgressive marine environment (Borg et al., 1960; Arbenz, 1989; Pitman et al., 1997). While the sand is well sorted and grains are sub-rounded at the optical scale, scanning electron microscopy reveals the sand grains to have a rough "brain-like" surface morphology (e.g., Elias and Hajash, 1992). Prior to experiments, the sand was cleaned in a dilute acid bath (5% HCl), washed with distilled water, and air-blown to remove fines (following the procedure of He, 2001). The sand was sieved to produce two different size fractions (124–180 and 250–350 μm).

Samples of the loose, granular sand were encased by silver foil soldered into cylindrical form and then jacketed by a heat-shrinkable poly-olefin or Teflon (PTE) tube. A thin wafer of Berea Sandstone (2.5 mm) was placed at the pore-fluid access port to prevent loss of sand grains into the pore-fluid system. During preparation of the sample assembly, the sand was gently vibrated so as to pre-compact the material and minimize the starting porosity. The mass of sand used for each experiment was determined by weighing on a digital balance, and these values were used to calculate starting porosities for our experiments (see Table 1). Prior to insertion of the sample assembly into the testing apparatus, air was evacuated from sample pore space and this was followed by injection of distilled water to pre-saturate the sand-pack.

2.2. Laboratory equipment

Hydrostatic and triaxial compaction experiments were performed in two screw-driven triaxial testing machines in the John Handin Rock Mechanics laboratory at Texas A&M University. Each apparatus provides different capabilities suitable to address particular goals of an experiment. One machine (LSR) is a variable strain rate, triaxial compression apparatus designed to deform specimens up to 5 cm diameter and 20 cm length at strain rates from 10^{-3} to 10^{-8} s^{-1}, at confining and pore-fluid pressures to 300 MPa, and at room temperature (Handin et al., 1972). The other is a modified variable strain rate triaxial compression apparatus (MVSR) designed to deform 2.5 by 6 cm samples at confining and pore pressures to 150 MPa, temperatures to 300 °C and strain rates from 10^{-3} to 10^{-8} s^{-1} (Heard, 1963).

Each apparatus subjects jacketed cylindrical samples to an external pressure imposed by a liquid confining media, and provides access to sample void space for the injection of distilled water pore fluid (see Fig. 1). For our experiments, sample lengths and diameters were 50 and 25 mm, respectively, for the LSR apparatus. The same dimensions for MVSR samples were 43 and 19 mm, respectively. Owing to the design of the sample columns, each apparatus utilizes slightly different jacketing materials that have slightly different stiffnesses. While these aspects have a measurable influence on the deformation character of the samples, the difference in the results obtained from each testing vessel is minor.

Throughout each experiment we monitored confining pressure (P_C), pore-fluid pressure (P_P), the axial loading force applied to the sample, axial shortening of the sample column, and the volume of the pore-fluid system. For experiments using the MVSR apparatus, we also monitored temperature and the number of

Table 1
Summary of experiment conditions and sample details

Experiment	Type of experiment	Grain size (μm)	Initial porosity (%)	Max. P_C (MPa)	P_P (MPa)	Axial strain rate (s^{-1})
LSR4492	Hydrostatic constant stress rate	124–180	32.6	262.5	12.5	–
MVSR029	Hydrostatic constant stress rate	250–350	31.1	42.5	12.5	–
MVSR031	Hydrostatic constant stress rate	250–350	31.7	87.5	12.5	–
MVSR030	Hydrostatic constant stress rate	250–350	31.5	137.5	12.5	–
LSR4475	Hydrostatic constant stress rate	250–350	34.0	200	12.5	–
MVSR016	Hydrostatic stress cycling	124–180	34.6	117.5	12.5	–
MVSR013	Hydrostatic stress cycling	250–350	31.3	117.5	12.5	–
MVSR027	Triaxial constant stress rate	250–350	32.1	75	12.5	1.5×10^{-5}
MVSR026	Triaxial stress cycling	250–350	31.8	75	12.5	1.5×10^{-5}

Karner et al. (2003) to be published in Tectonophysics.

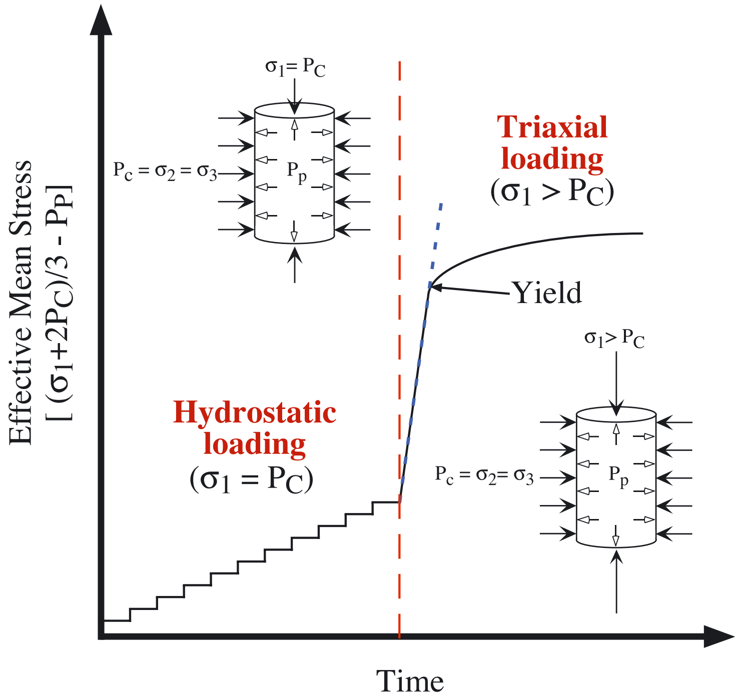

Fig. 1. Schematic diagram illustrating the loading paths for hydrostatic and triaxial compaction experiments.

acoustic emissions. Pressures were maintained to within ± 0.5 MPa using HIP pressure actuators. For each apparatus, a constant axial strain rate (1.5×10^{-5} s^{-1}) was induced by a motor acting on the gear-driven screw mechanism. Pore-fluid volume was monitored to within 5×10^{-5} cc using a displacement transducer connected to the pore pressure HIP piston.

2.3. Acoustic emission system

One apparatus used for the experiments described here (the MVSR) is equipped with a piezo-ceramic transducer to detect acoustic emissions (AE) produced during sample deformation. The raw signal from the piezo-ceramic acoustic emission detector was sent to electronic circuitry designed to amplify, band-pass filter (between 4 and 400 kHz), and integrate the incoming waveforms (Lenz, 2002). The integrated waveform was then sent to computer for software counting of the acoustic pulses. A software threshold is compared to pulse lengths and amplitudes of incoming waveforms to discriminate actual microseismicity from electrical noise.

At the start and end of each experiment, we monitor the system at ambient room pressure and temperature conditions to determine the background noise level of the AE system. The background noise rates we observe are usually less than 20 counts per hour and most typically around 10 counts per hour. Even for the lowest pressures applied during deformation, the AE rates we record are typically not less than ~ 100 counts per hour. Thus, the background AE noise level is low when compared to the total number of AE recorded. We infer that the recorded background noise persists at a constant rate throughout an experiment. This constant noise rate is determined for each experiment and is subtracted from the AE data collected during sample deformation.

The experiments reported here utilized an early design of our AE detector (which has since been modified). Owing to the sample column configuration, the coupling of the AE detector to the loading piston varies somewhat between experiments. Thus, the absolute numbers of AE events recorded for separate experiments can only be compared to first order. Yet, the AE data obtained for any given experiment are internally consistent and meaningful because the detector coupling does not vary during a test.

2.4. Experiment procedure

For purposes of reproducibility, we employed an identical start-up pressurization sequence for all experiments. Confining pressure was initially raised to 0.4 MPa while the pore-fluid system was drained and maintained at atmospheric pressure. In this way, pressure leaks across the sample jacketing could be readily identified. Subsequent pressurization occurred with the pore-fluid system closed and stepping both the confining and pore-fluid pressures by 0.4 MPa every 90 s. In this way, a constant effective pressure (P_E) was maintained until the initial experiment pressures were achieved ($P_C = 15.0$ MPa, $P_P = 12.5$ MPa). For better comparison between experiments, we select these starting conditions to be our zero reference for measurements of pore-fluid volume change that occur during sample deformation. Throughout each experiment, pore-fluid pressure was kept at the starting level of 12.5 MPa and we monitored the change in fluid volume needed to maintain constant pressure. We calculate volumetric strain by normalizing the measured change in fluid volume by the calculated bulk volume of the sample at the start of the experiment. We then consider this volumetric strain to be a proxy for the change in sample porosity.

Two modes of imposing stress were employed for our experiments (as shown in Fig. 1). All samples were subjected to an initial stage of hydrostatic stressing in the absence of an extra axial load (i.e. $\sigma_1 = P_C$). For some experiments, after a target effective pressure was achieved samples were subjected to triaxial (or non-hydrostatic) stressing through the application of an extra axial load. We have performed four different types of experiments to investigate how strain can be accommodated during deformation of granular quartz sand:

1. hydrostatic constant stress rate tests for which effective pressure was monotonically increased to a target maximum level (e.g. Figs. 1–4), achieved by stepping confining pressure at a constant rate and maintaining pore pressure constant;
2. hydrostatic stress cycling tests for which effective pressure was increased as above, but was periodically decreased to the starting conditions (e.g. Fig. 5). For successive reloading cycles, effective pressure reached increasingly greater levels than that to which the sample had previously been subjected;
3. a triaxial deformation test for which effective pressure was first monotonically increased to a target value of 62.5 MPa. Then the sample was shortened by axial loading at a constant strain rate (e.g. Figs. 1 and 6);
4. a triaxial stress cycling test for which effective pressure was first monotonically increased to a target value of 62.5 MPa. Then, repeated cycles of axial straining were imposed to subject the sample to greater levels of stress and, hence, deformation (e.g. Fig. 7).

To determine experiment reproducibility and to explore the generality of our observations, we performed tests on two size fractions of St. Peter quartz sand (124–180 and 250–350 μm). The salient details about these experiments are listed in Table 1.

2.5. Terminology used

We adopt the nomenclature commonly used by the Rock Mechanics community, rather than that reported in the Engineering and Material Science literature. For example, compressive stresses and compactive volumetric strains are taken to be positive (see Fig. 1). As our sand samples were deformed in the presence of pore fluid, we use the difference between the applied confining and pore pressures to define an effective pressure ($P_E = P_C - P_P$; also referred to as 'differential pressure' in soil mechanics).

For samples subjected to an extra loading force along the cylindrical axis (e.g. Fig. 1), we take the difference between the applied axial stress and confining pressure as differential stress ($\Delta\sigma = [\sigma_1 - P_C]$, also known as the 'deviator stress' in engineering). When the applied axial stress, confining pressure and pore-fluid pressure are taken collectively they define an effective mean stress ($\bar{\sigma}_{\mathrm{eff}} = [\sigma_1 + 2P_C]/3 - P_P$). It can be seen from these combined relationships that when differential stress is zero then effective mean stress is equal to the hydrostatic effective pressure.

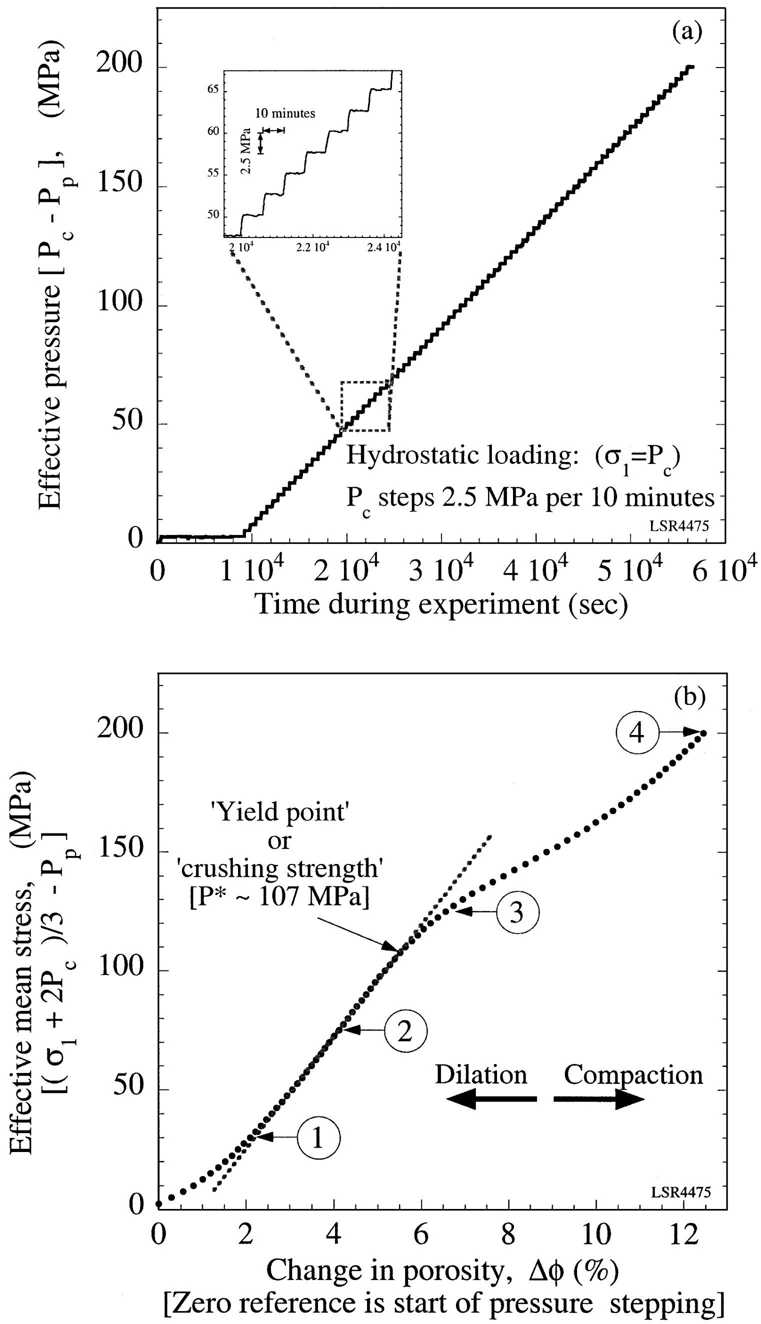

Fig. 2. Hydrostatic constant stress rate experiment performed in the higher pressure LSR apparatus. (a) Effective pressure plotted as a function of time. Inset shows the stressing rate imposed on the sample. (b) Stress–strain curve for the deformed granular sand. Volumetric strain (which is cast in terms of porosity change) was measured throughout. Porosity differences are referenced to the starting conditions at $P_E = 2.5$ MPa. For clarity, we plot the porosities measured at the end of each 10-min pressure step. Also indicated by the numbers 1–4 are maximum pressures for a series of identical hydrostatic experiments from which we have performed microstructural analyses (see Fig. 4).

Thus, by casting the applied load in terms of effective mean stress ($\bar{\sigma}_{\text{eff}}$), results from experiments involving either hydrostatic or triaxial loading modes can be compared directly.

3. Results

The results from our experiments are presented in Figs. 2–7. For each case, samples exhibit behaviour

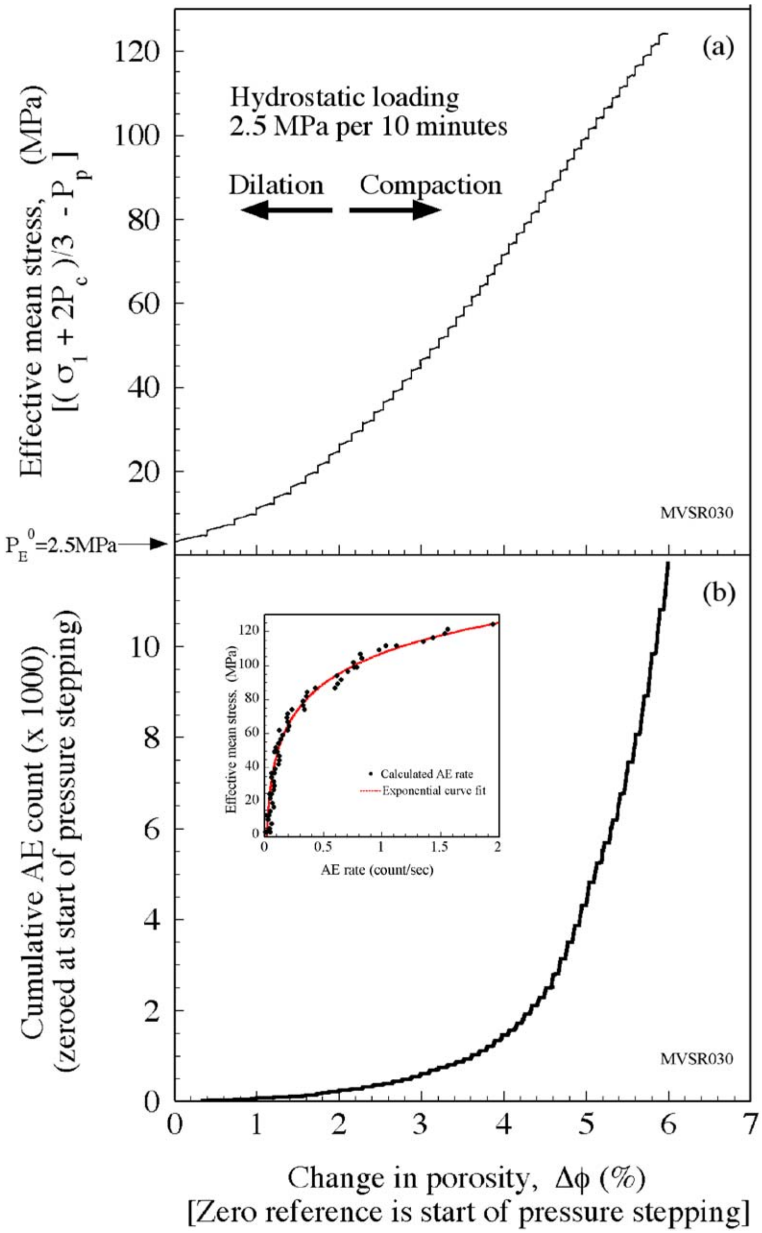

Fig. 3. Data from a hydrostatic constant stress rate experiment performed to $P_E = 125$ MPa in the lower-pressure MVSR apparatus. Steps in the data reflect the sample response to individual increments of effective pressure. (a) Stress–strain curve recorded during deformation of the granular sand. (b) Acoustic emission data for the same MVSR stress–strain experiment shown in (a). The main plot displays the cumulative AE count recorded during sample deformation, while the inset figure shows the AE rate determined for this test.

similar to elasto-plastic deformation with macroscopic yielding above a critical mean stress. Yet as we will demonstrate, the style of deformation for cohesionless, granular sand is not so straightforward. This is because deformation occurs through a variety of elastic and inelastic mechanisms that operate simultaneously for the conditions that we studied.

3.1. Constant stress rate tests

Results from hydrostatic experiments show that loose, granular sands compact as effective pressure is increased. However, compaction rates display considerable variation as a function of the applied stress, with a characteristic sigmoidal relationship between stress and volumetric strain (recast as porosity in Fig. 2). At low effective pressures (less than 20 MPa for the experiment data shown in Fig. 2b), significant compaction occurs with a gradual transition to lower compaction rates as effective pressure increases. For intermediate effective pressures (between 40 and 100 MPa in Fig. 2b), the stress–porosity curve becomes quasi-linear giving the appearance of an elastic response to loading. At even greater loads, a second stage of increased compaction rate occurs that closely resembles compactive failure of granular media (e.g. Zhang et al., 1990a,b) marking the onset of pervasive inelastic grain failure at a critical effective pressure (denoted by P^*). For the grain size range that we tested (250–350 μm), P^* was observed to be ~ 107 MPa.

Inelastic strain prior to P^* is revealed by acoustic emissions that occur during sample deformation (Fig. 3). We monitored volumetric strain and acoustic emissions for the hydrostatic deformation of sample MVSR030 to an effective pressure of 125 MPa (Fig. 3a), slightly greater than the crushing strength determined from sample LSR4475 ($P^* \sim 107$ MPa in Fig. 2b). The cumulative number of acoustic emissions is significant, and AE rates increase in a nonlinear manner as the applied pressure is increased (Fig. 3b). At low stresses where strains are large, the cumulative number of AE is small and the AE rate is low. The number of AE increases with effective pressure and the AE rates accelerate significantly for pressures above ~ 60 MPa, revealing that considerable inelastic deformation occurs well before the conventional macroscopic yield stress is reached, as denoted by P^* (Figs. 2 and 3). This is consistent with results from hydrostatic compaction experiments on sandstones that show increased AE rates near P^* and maximum AE rates in the post-failure region of the loading curve (Zhang et al., 1990b).

Post-experiment observations of our samples show that significant grain size reduction occurs at pressures above P^*, consistent with previous work on sandstone (e.g. Zhang et al., 1990a). However, we observe considerably less fragmentation and grain size reduction at pressures below P^*. In Fig. 4, we show transmitted light micrographs from samples that were deformed to different levels of effective pressure (as shown by the numbers 1–4 in Fig. 2b). For comparison, we show an image of the pre-experiment starting material (Fig. 4a). The sample deformed to low pressure ($P_E = 30$ MPa; Fig. 4b) shows that while a small number of new intragranular fractures have formed there are few indications of significant transgranular fractures or grain fragmentation. At slightly higher pressure but less than P^* ($P_E = 75$ MPa; Fig. 4c), we observe a significant increase in fracture density with the presence of some transgranular fractures and grain fragmentation. At a pressure slightly above P^* ($P_E = 125$ MPa; Fig. 4d), the samples show clear evidence of widespread fracturing, fragmentation and grain size reduction. At the highest pressure we tested ($P_E = 200$ MPa; Fig. 4e), the sample displays extreme amounts of fragmentation with far fewer intact grains having survived the experiment. Thus, the progression of images (Fig. 4a–e) qualitatively shows a nonlinear increase in fracture density and fragmentation in a manner consistent with the accelerating AE rates shown in Fig. 3. This compares well to quantitative microstructural analyses from creep compaction experiments on St. Peter quartz sand performed at similar pressures to the deformed samples shown in Fig. 4 (Chester et al., in press).

3.2. Hydrostatic stress cycling tests

The departure from simple elastic behaviour at subcritical pressures is revealed further by hydrostatic stress cycling experiments (Fig. 5). Samples of St. Peter sand were loaded to a target effective pressure at the same stressing rate as before (i.e. 2.5 MPa every 10 min), followed by intervals of unloading for which

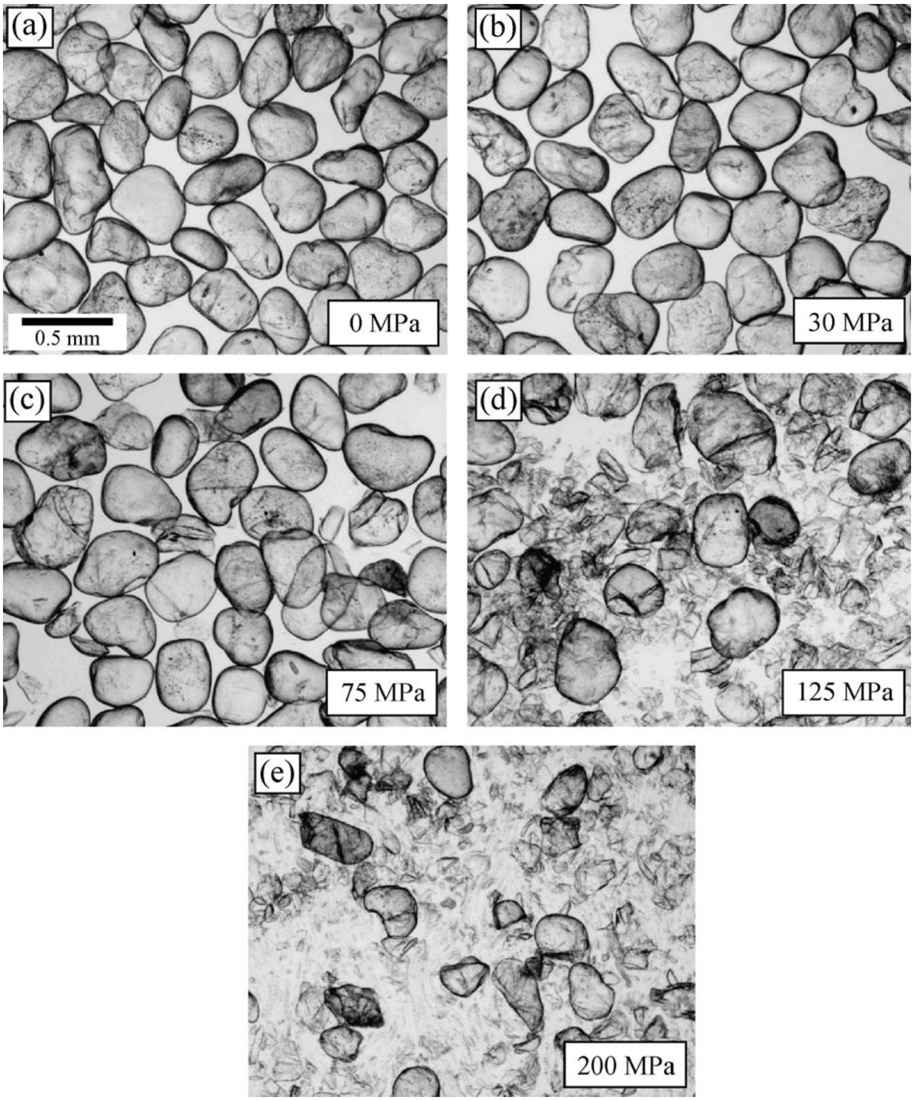

Fig. 4. Transmitted light photomicrographs of St. Peter quartz sand immersed in mineral oil. The images show an increase in fracture density and fragmentation as a function of effective pressure. Samples were obtained from constant stress rate hydrostatic experiments with the maximum effective pressures as shown in Fig. 2b. Images were obtained using the same magnification; the scale bar shown in (a) is 0.5 mm and applies to all photomicrographs. (a) Starting material; (b) maximum $P_E = 30$ MPa; (c) maximum $P_E = 75$ MPa; (d) maximum $P_E = 125$ MPa; (e) maximum $P_E = 200$ MPa.

confining pressure was reduced to the starting level of 15 MPa (effective pressure of 2.5 MPa). Samples were reloaded to a new pressure that exceeded the level of the previous loading cycle (Fig. 5a), then subsequently unloaded. These stress cycles were repeated multiple times to ever increasing levels of applied pressure. To remain consistent with studies from soil mechanics, we denote the peak stress level of the prior loading cycle as ‘‘previous maximum mean stress’’ (or PMMS).

At low-effective pressures, the initial volumetric strain rates for each reload curve are large and the rates subsequently decrease at higher pressures. Thus, each loading curve exhibits concave upwards charac-

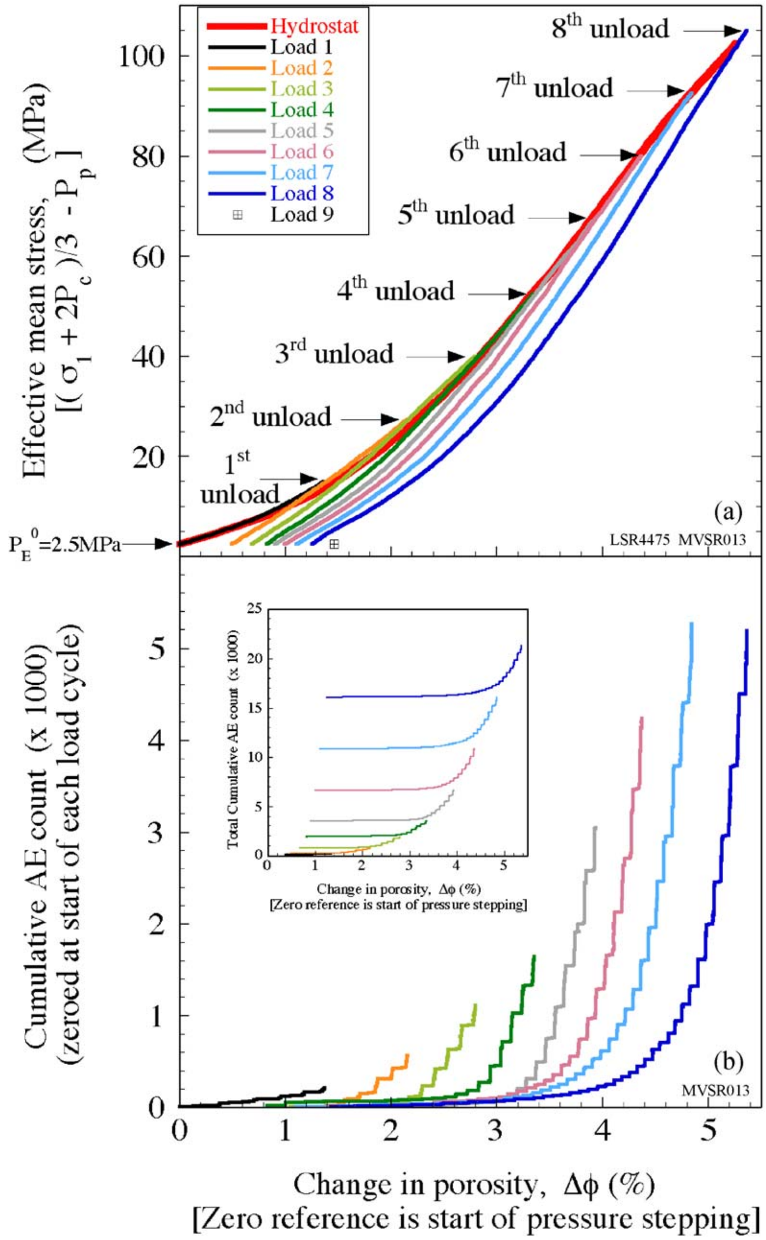

Fig. 5. Results from a hydrostatic stress cycling experiment. (a) Stress–strain measurements at the end of each 10-min interval are shown for the stress cycling experiment. Separate loading cycles are marked by increasing levels of effective pressure and the successive offsets in volumetric strain. For comparison, these are superimposed on the data from the constant stress rate test (from Fig. 2b). (b) The cumulative AE count is shown for each loading cycle in (a). AE count has been zeroed at the start of each stress cycle. Inset figure shows the total cumulative AE recorded for the experiment.

ter at low pressures which gradually becomes quasi-linear as effective pressure increases. In this way, the general character of reloading curves mirrors the behaviour observed from the constant stress rate experiments. However, permanent strain increases with each successive loading cycle and the reloading curves fall below an upper bound defined by the hydrostatic constant loading rate curve (replotted from Fig. 2b).

The reloading curves can also be distinguished from the constant loading rate curve by several additional differences. First, the amount of volumetric strain during the low-pressure portions of each reloading cycle is less than that observed from the hydrostat curve. Second, for stresses below the PMMS the reloading curves display a quasi-linear section with a steeper slope than the comparable portion of the hydrostat curve. Third, when effective pressure nears (or exceeds) the PMMS the reloading curve slopes decrease slightly and more closely resembles the hydrostat data (taking the form of a secondary yield). These systematic observations reveal that significant inelastic strain processes operate at sub-critical pressures (i.e. below P^*).

Cumulative acoustic emissions recorded during each sequential loading (Fig. 5b) exhibit similar character to AE from a constant loading rate experiment (Fig. 3b). For easier comparison between successive load cycles, we reset the AE count to zero at the start of each reload cycle. AE activity is minimal at low-effective pressures, and AE rates increase with effective pressure in a nonlinear manner. The total AE count that occurs during unloading is small (typically only tens of events) and these are clustered near the high-pressure region at the start of each unload. Upon reloading, AE rates are initially very low and only increase when the imposed effective pressure approaches the level achieved in the previous stress cycle (PMMS). For each reload, AE rates are significantly large when the applied pressure exceeds the PMMS.

The systematic observations of volumetric strain and AE activity indicate that non-recoverable strain mechanisms operate at all stress conditions studied. If the large AE rates at elevated pressure correspond with the post-experiment observations of particle size reduction, then the measured AE may represent microseismicity from grain cracking and breakage. Yet, we recognize that AE may also be generated via frictional slip at grain contacts. In either case, large AE rates would correspond to increased volumetric strains when loading stresses exceed the PMMS (or even P^*). However, the low numbers of AE at low stresses suggests a different strain mechanism than that which occurs at higher stress (i.e. grain breakage). This indicates that several deformation modes operate during hydrostatic stressing of granular media. Yet, it raises the question of how strain will be accommodated when samples are subjected to more complicated stress states—such as during non-hydrostatic (or triaxial) deformation.

3.3. Non-hydrostatic (triaxial) deformation tests

We investigated non-hydrostatic compaction of St. Peter quartz sand by performing a triaxial deformation experiment at an effective pressure well within the quasi-linear portion of the hydrostatic loading curve. During the first stage of the experiment, the sample was hydrostatically loaded at a rate of 2.5 MPa per 10 min to a target effective pressure of 62.5 MPa (Fig. 6a). In the second stage of deformation, the sample was axially loaded at a strain rate of 1.5×10^{-5} s^{-1}.

The hydrostatic portion of the loading curve (Fig. 6) is consistent with our results shown in Figs. 2–5 in terms of the deformation character and amount of sample compaction. From an initial effective pressure of 62.5 MPa, samples are further compacted under triaxial loading. The stress–strain curve resembles the characteristic behaviour of a material that yields in compression (e.g. Brace, 1978; Zhang et al., 1990a; Brzesowsky, 1995; see Fig. 1). That is, the initially quasi-linear loading curve is followed by yielding for which large strains are induced by small increments in triaxial stress (plotted in terms of effective mean stress in Fig. 6). The hydrostatic portion of the experiment data shown in Fig. 6b records a similar number of acoustic emissions to our hydrostatic results that we described previously. Furthermore, the nonlinear increase in AE activity with increasing hydrostatic stress is also consistent with our previous observations.

Despite the similar mean stresses imposed, however, there are striking differences between hydrostatic and triaxial deformation that are accentuated by the measured AE (Fig. 6). Triaxial deformation is associated with lower ultimate strengths and greater volumetric strains than observed from hydrostatic deformation tests. Furthermore, the AE rates monitored during triaxial deformation are significantly greater than the rates obtained from hydrostatic stressing tests. AE rates increase as triaxial loading pro-

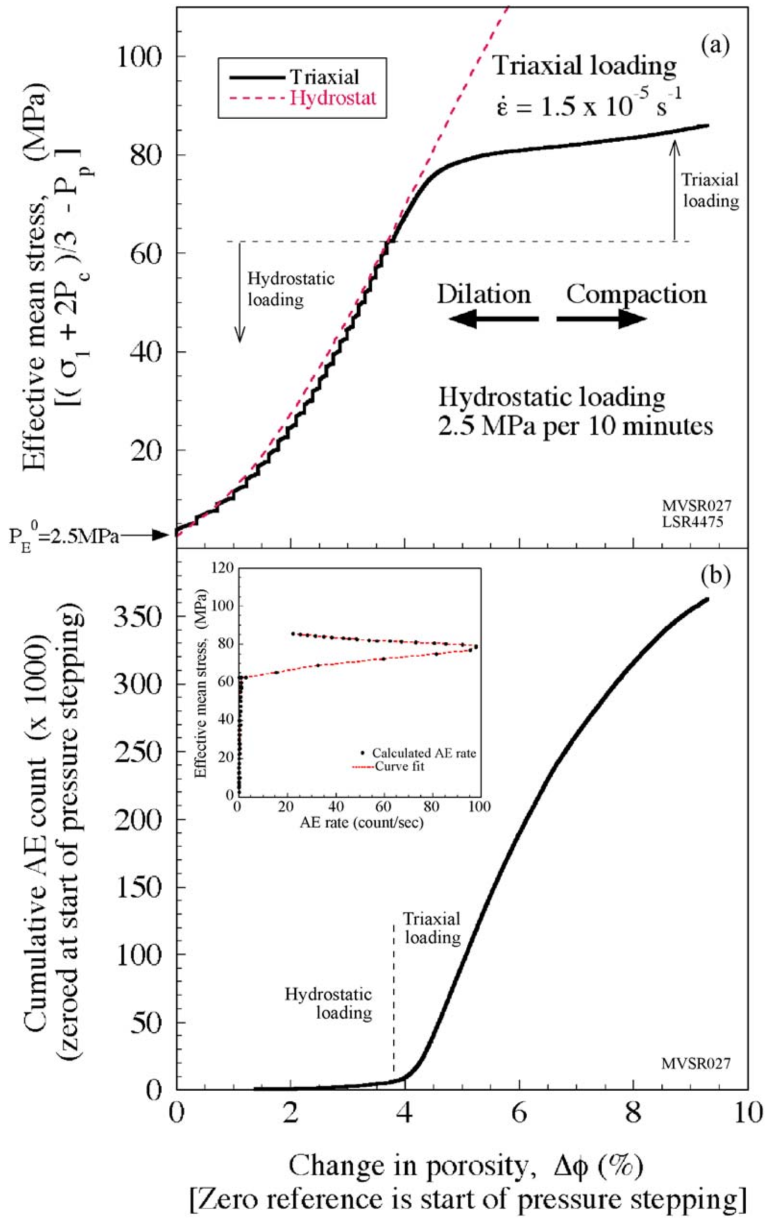

Fig. 6. Results from a triaxial experiment. The sample was initially stressed hydrostatically to an effective pressure of 62.5 MPa, followed by application of differential stress. (a) Stress–strain data recorded during sample deformation. The hydrostatic and non-hydrostatic portions of the test are as labelled. For comparison, we replot data from the hydrostatic loading test of Fig. 2. (b) The main plot shows the cumulative AE count recorded for the deformation results shown in (a). Inset figure shows the AE rate determined for this test.

ceeds and are maximum in the post-yield portion of the stress–strain curve shortly after yield. AE rates decrease towards a background level as post-yield triaxial loading continues.

3.4. Non-hydrostatic stress cycling tests

Inelastic response prior to macroscopic critical failure is also observed from triaxial stress cycling experiments (Fig. 7). We deformed St. Peter sand under the same triaxial conditions as the experiment shown in Fig. 6, except that during the non-hydrostatic portion we periodically imposed triaxial stress cycling. After axial stress was increased to a prescribed level, the sample was unloaded to the

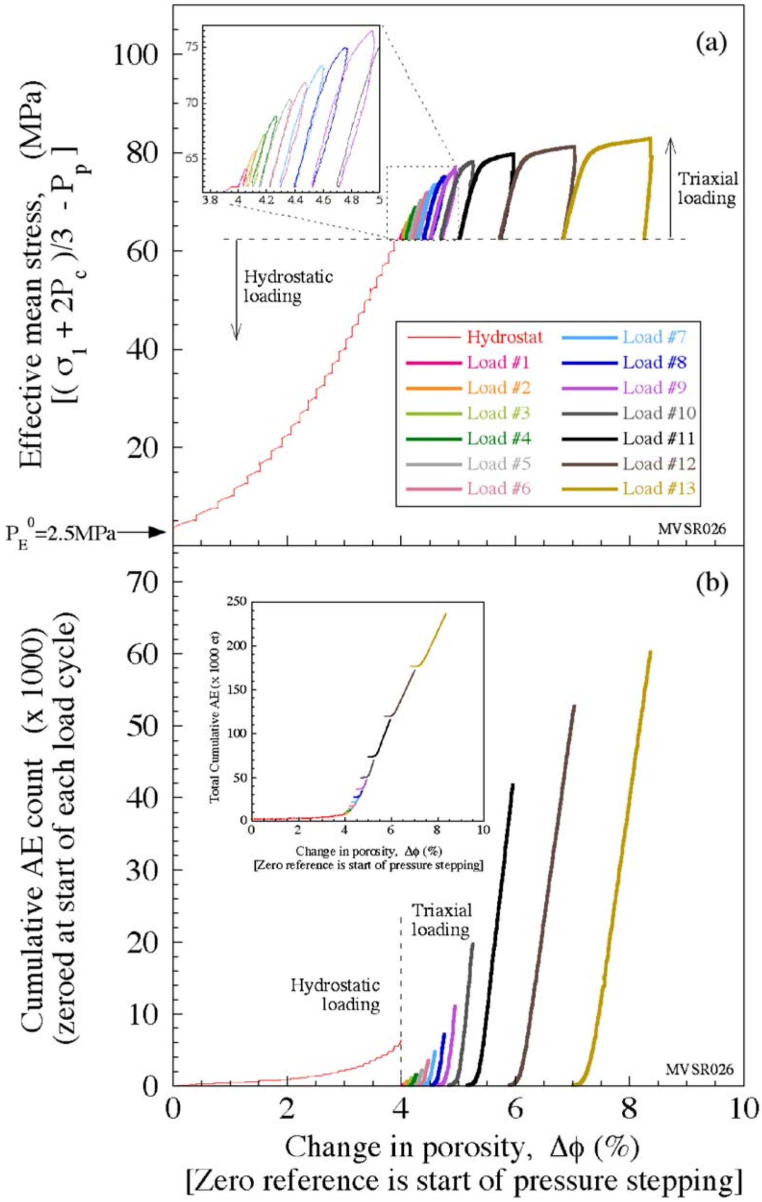

Fig. 7. Results from a triaxial stress cycling experiment. The sample was stressed in a manner similar to the test in Fig. 6, except that for triaxial loading the differential stress was periodically reduced to zero. (a) Stress–strain data obtained during sample compaction. Inset figure shows an expanded view of the first nine loading cycles. (b) Cumulative AE count recorded for the test shown in (a). AE data were zeroed at the start of the hydrostatic and non-hydrostatic portions, as well as at the start of each stress cycle. Inset figure shows the total cumulative AE for this experiment.

maximum hydrostatic stress level (62.5 MPa) by reversing the direction of the axial loading piston.

In a manner similar to our hydrostatic stress cycling experiments, data from our triaxial stress cycles indicate that the deformation response is not purely elastic (Fig. 7). With successive stress cycles, volumetric strains increase with significant offsets from the previous loading cycles. These offsets are measured for the first few loading cycles in the sequence, indicating that permanent strains are apparent even for the lowest axial stress imposed. Moreover, a comparison of loading curves reveals that greater volumetric strains result from triaxial stress increments than from hydrostatic stressing. For example, the first three triaxial load cycles indicate a permanent porosity loss of $\sim 0.02\%$ per MPa of applied mean stress, compared to permanent volumetric strains of $\sim 0.007\%$ per MPa during hydrostatic stressing.

This is further accentuated by AE events which become more numerous and correspond to larger increments in volumetric strain with successive loading cycles (Fig. 7b). These observations agree with results from triaxial experiments that show a qualitative correlation between macroscopic yield and maximum AE rates for sandstones (e.g. Zhang et al., 1990a) and soils (Lord et al., 1977). Yet, there are differences between the AE recorded from hydrostatic experiments and those data from triaxial stress cycling tests. First, the AE from triaxial stress cycles are generally more numerous and occur at higher rates than for hydrostatic loading (compare Figs. 5b and 7b, each having $\sim$6,000 AE events for hydrostatic loading to 62.5 MPa). Second, the AE from triaxial stress cycles show sharper transitions to faster rates than observed from the hydrostatic test. Thus, inelastic mechanisms are seemingly more sensitive to triaxial stresses than to hydrostatic loading conditions.

4. Discussion

The mechanical response we have measured for St. Peter sand is qualitatively similar to previous work on other granular media and analog materials (e.g. Borg et al., 1960; Gallagher et al., 1974; Zoback and Byerlee, 1976; Brzesowsky, 1995; Dewers and Hajash, 1995; Olgaard et al., 2001; Chuhan et al., 2002), on loose soils (e.g. Schofield and Wroth, 1968; Britto and Gunn, 1987; Bridgwater, 1994), and on cohesive, cemented granular rocks such as sandstone (e.g. Zhang et al., 1990a,b; David et al., 1994; Wong et al., 1997; Baud et al., 2000). Taken collectively, these data highlight the complexities of deformation within granular materials. While soil mechanics studies provide an extensive dataset for granular deformation, they are typically performed at lower pressures than their counterparts from rock mechanics. This is important because it is frequently assumed in soil mechanics research that grains are unbreakable and that deformation is accommodated by granular rolling, grain-contact frictional slip, or elastic distortion of the stressed grains (Gudehus, 2000; Walker, 2000). This assumption forms the foundation for elasto-plastic and hypoplastic constitutive models used to describe soil deformation (e.g. Herle et al., 2000; Marcher et al., 2000). As our samples were subjected to stresses near or above the fracture strength of individual grains, constitutive models for soils cannot account for all the grain-scale processes that occur during our experiments (as noted by Brzesowsky, 1995).

4.1. Comparison to results from soil mechanics

Deformation studies of soils have often noted a nonlinear response to loading (e.g. Terzaghi, 1925; Biot, 1941, 1973; Britto and Gunn, 1987; Bridgwater, 1994). Loading curves from these studies are frequently presented in terms of the logarithm of stress (e.g. Graham and Hovan, 1986; Ramsamooj and Alwash, 1990; Smith et al., 1992). This serves to minimise the nonlinear character of the loading curves for the range of stresses considered in soil mechanics (typically of the order of 10s of kPa up to $\sim$10 MPa). This loading behaviour corresponds favourably to the nonlinear character observed from the deformation of St. Peter sand at low stresses (see Figs. 2–7). While elastic models predict stress-dependent curvature at low stresses (e.g. Hertz, 1881; Mindlin and Deresiewicz, 1953), the nonlinearity observed during soil deformation is often attributed to inelastic consolidation processes.

Stress cycling tests that deform soils at low stresses (< 1 MPa) exhibit non-recoverable (or permanent) strains that are consistent with post-yield behaviour (Smith et al., 1992). In those tests, increased loading delineates a line of 'normal' consolidation which correlates to the low-pressure hydrostatic loading of our experiments (e.g. Figs. 2–5). The unloading during stress cycles exhibit steeper stress–strain curves than that of 'normal' consolidation, to the extent that strain is not fully recovered upon complete removal of stress (similar to Fig. 5). The reloading path exhibits this steep character until the applied stress exceeds the previously applied pressure, much as observed in our experiments once PMMS is reached. At this point, the loading path shallows and resumes the trend of the "normal" consolidation line. This takes the appearance of yielding of the material. Similar results have been reported for stress cycling tests performed on oceanic sediments (Olgaard et al., 1995, 2001).

Yielding in soils is typically described as the transition from elastic to plastic behaviour (Britto and Gunn, 1987; Smith et al., 1992). For our experiments, this might be considered to occur near the point marking the onset of pervasive grain crushing and cataclastic flow, P^* (e.g. Zhang et al., 1990a). Yet, our stress cycling experiments indicate that permanent strains occur at much lower stresses than P^*. Similar studies from soil mechanics have identified a more elaborate and complex scheme to describe yield surfaces (Smith et al., 1992). This scheme involves four stages of deformation that are loosely consistent with concepts in rock mechanics. In the first stage, soils exhibit linear elastic behaviour with completely reversible strain up to a 'yield' stress level analogous to an elastic limit. In the second stage, strains are still recoverable but the loading path becomes nonlinear providing an apparent decrease in material stiffness. The third stage is marked by the onset of non-recoverable strain, a feature considered to define material yield. Permanent strains increase in magnitude during this stage as the applied stresses become greater. This third stage is limited by the failure envelope for the soil which, in turn, corresponds to an abrupt and significant change in volumetric strain rates. The fourth, and final, stage is marked by deformation in what can be considered as a 'post-failure' region. However, it must be recognized that each of these stages is restricted by limits that each, in their own way, conveys a different concept of yielding. We shall adopt the classic definition of yield, which is marked by the onset of permanent strain (i.e. the point between stage 2 and 3 deformation).

For unconsolidated soils, the onset of permanent strain during third-stage deformation typically occurs at stresses lower than the initial conditions of our experiments. This, coupled with observations from our stress cycling experiments (e.g. Figs. 5 and 7), implies that the behaviour exhibited by our samples is not achieved solely by elastic deformation. Thus, from a soil mechanics perspective our samples always exhibit yield over the range of stresses that we report here.

4.2. Comparison to deformation experiments on sandstone

The loose, granular quartz sand of our experiment samples did not have the cohesion brought about by natural processes such as consolidation, inter-granular cementation, and mineral diagenesis. Yet, the form of our stress–strain curves is very similar to the character observed for deformation of naturally lithified quartz sandstones (e.g. Zhang et al., 1990a,b; David et al., 1994; Wong et al., 1997; Baud et al., 2000). Zhang et al. (1990a,b) characterized a variety of sandstones in terms of mean grain size (d) and average porosity (ϕ) and showed that these microstructural parameters can be related to the critical compaction that occurs at P^*. Superimposed on their loading data for sandstones we show our results from hydrostatic deformation of loose, quartz sand (Fig. 8). The mean grain size and starting porosity for our experiments are within the range studied by Zhang et al. (1990a).

The loading curves for both loose sand and lithified sandstone exhibit relatively large strain rates when pressure is initially applied, followed by a transition to steeper, quasi-linear loading behaviour prior to the second interval of large strain rates associated with P^*. From their results for sandstones, Zhang et al. (1990a,b) note that this second transition corresponds to significant micro-cracking at grain contacts, which is supported by increased acoustic emission rates that are maximum in the post-yield portion of the loading curve (Zhang et al., 1990b; David et al., 1994). From this, it is concluded that P^* marks the onset of pervasive grain fracturing leading to significant sample compaction (Wong et al., 1997). Our observations for this transition in loose sands are similar to those for sandstone (Fig. 2) and are supported by microstructural observations of our samples (Fig. 4). Yet, it

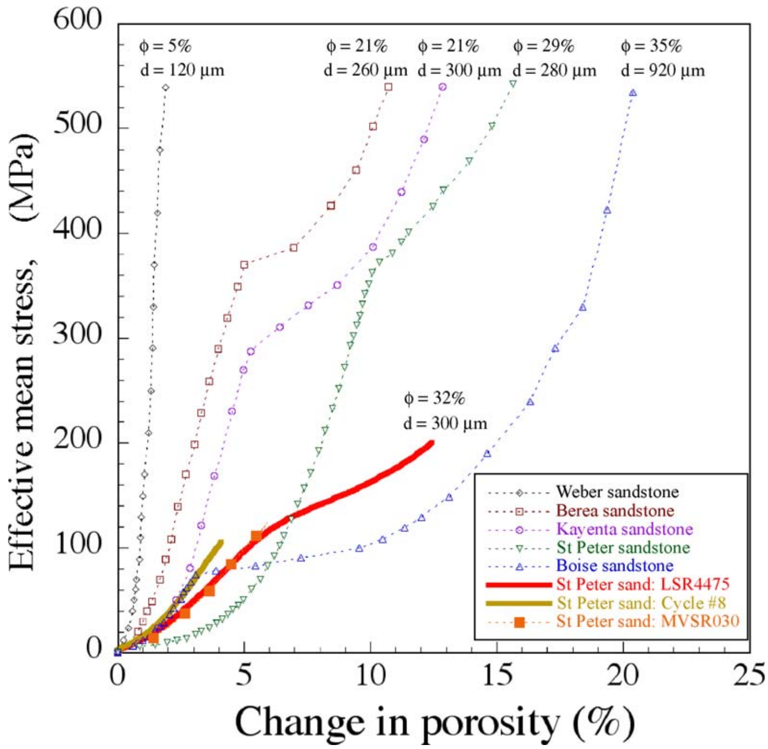

Fig. 8. Comparison of our hydrostatic experiments for St. Peter sand to results for sandstones. We compare our constant stress rate results (from Figs. 2b and 3a) and the final loading path from our hydrostatic stress cycling experiment (from Fig. 5a) with sandstone data from Zhang et al. (1990a). It is important to note that our samples were deformed at a constant stress rate, whereas the sandstones were deformed at variable stressing rates.

is clear from the comparison in Fig. 8 that there are significant differences.

The crushing strength (P^*) of St. Peter sand is generally lower than P^* observed for consolidated sandstones of similar grain size and porosity, particularly when compared to Berea, Kayenta, and St. Peter sandstones (Zhang et al., 1990a). The crushing strength for St. Peter quartz sand (grain size 250–350 μm; $P^* \sim 107$ MPa in Fig. 2) is of the same order as that reported for deformation of loose Ottawa quartz sand having slightly larger grain diameter and broader size distribution ($P^* \sim 65$ MPa from Zoback and Byerlee, 1976). When compared to the sandstones, however, we note that Boise sandstone exhibits a lower crushing strength than for our sand samples. Boise sandstone has porosity similar to our starting material, yet it has a much larger mean grain size (560 and 920 μm for two samples measured by Wong et al., 1997). This is consistent with previous work showing that P^* decreases for samples consisting of larger grains and having greater porosity (Zhang et al., 1990a; Wong et al., 1997) and a companion study in which we have investigated grain size effects (Karner et al., 2001, submitted for publication). In addition to grain size and porosity, though, the character of grain contacts in sandstones will differ from loose sands due to processes such as cementation and grain suturing. Furthermore, other parameters (e.g. grain angularity, compositional heterogeneities) may alter the macroscopic strength behaviour of granular sands. As yet, it remains to be seen exactly what influence these factors would have on P^*.

The sand and sandstone results presented in Fig. 8 also show variations in the slope of the stress–strain curves. These slopes provide a measure of effective material stiffness, or bulk compressibility (Zimmerman, 1991). At stresses below P^*, the effective stiffness of quartz sand (replotted from Figs. 2 and

3) is significantly lower than those of the sandstones. Yet, this discrepancy is reduced if we compare the effective stiffness for stress cycle #8 to the sandstone data. The sand data from the stress cycle coincide well with the sub-critical loading curve for Boise sandstone. If sandstones are considered to be a consolidated version of our loose sands, then the steep curve for stress cycle #8 may reflect a high consolidation state brought about by grain rearrangement during earlier loading cycles.

For sub-critical stresses below P^*, it has been assumed that strains in sandstones are accommodated by elastic deformation of grains (not through inelastic mechanisms) because sandstones are comprised of a cohesive framework of individual grains (Zhang et al., 1990a; Wong et al., 1997; see Fig. 8). This assumption is primarily based on the character of the loading curve which shows a transition to quasi-linearity with increased applied load. This implies that for purely elastic sub-critical deformation of sandstones, intergranular cohesion is not altered as the applied stress is increased. Yet, acoustic emission data from experiments on sandstones show significant AE rates for sub-critical pressures well below P^* (Zhang et al., 1990b; David et al., 1994; Wong et al., 1997). If this microseismicity is associated with deformation at grain contacts (e.g. breaking of intergranular cement) then the sandstones might undergo a measurable amount of permanent strain. Thus, it remains to be verified whether sub-critical deformation of sandstones occurs purely through elastic mechanisms.

4.3. Recoverable versus permanent strain

Our experiments on cohesionless quartz sand show that the relative contributions from elastic and permanent deformation mechanisms are difficult to resolve when samples are subjected to monotonically increasing stresses. Stress cycle tests on soils (e.g. Terzaghi, 1925) and our sand samples (Figs. 5 and 7) show that permanent strain accumulates at all stresses imposed on the sample. On the basis of soil and rock mechanics studies, we should expect deformation of cohesionless granular media to occur via particle rolling, frictional sliding, grain rotation, and grain fracture. Such granular rearrangement mechanisms produce an improved degree of consolidation (e.g. Hedberg, 1926; Athy, 1930; Graton and Franser, 1935; Maxwell, 1964), which increases sample stiffness and lowers compressibility (e.g. Zimmerman, 1991).

To investigate the stress dependence of consolidation, we analyse our experiments in terms of a compressibility that can be calculated directly from our measurements (Fig. 9). Compressibility (C), the reciprocal of stiffness, is a measure of the volumetric strain resulting from an applied change in pressure. For a porous media, there are four different compressibilities that can be determined from two independent volumes (pore space, V_P; and total or bulk sample volume, V_b), the applied pore pressure (P_P) and confining pressure (P_C) (Zimmerman, 1991). For our experiments, the measured change in fluid volume that is needed to maintain pore pressure reflects the evolution of pore volume (V_P) brought about by pressure-dependent sample compaction. This can be used to determine pore compressibility, as described by:

$$C = \frac{-1}{V_P^i}\left[\frac{\Delta V_P}{\Delta P_C}\right]_{P_P} \tag{1}$$

where V_P^i is the initial reference pore volume, the subscript P_P indicates that pore pressure is maintained constant, and the negative sign accounts for sample compaction (pore volume loss) with increasing confining pressure.

In Fig. 9a, we show calculated pore compressibilities for the stress cycling experiments (Fig. 5a). For comparison, we plot the calculated values for each loading curve together with the pore compressibility determined from the hydrostatic constant stress rate test (from Fig. 2). For each case, pore compressibilities are greatest at very low-effective pressures. As stress increases, pore compressibility decreases to a minimum value at stresses just below the crushing strength (P^*). At P^*, pore compressibility exhibits a marked increase. While compressibilities for each loading cycle display similar pressure-dependent character, distinct variations in the compressibility curves are apparent.

First, stress cycle compressibilities are generally lower than those calculated for the constant stress rate test. To clarify this point, we have determined the minimum compressibility for each load cycle as a function of previous maximum pressure (PMMS) and compare these to the calculated values for the constant

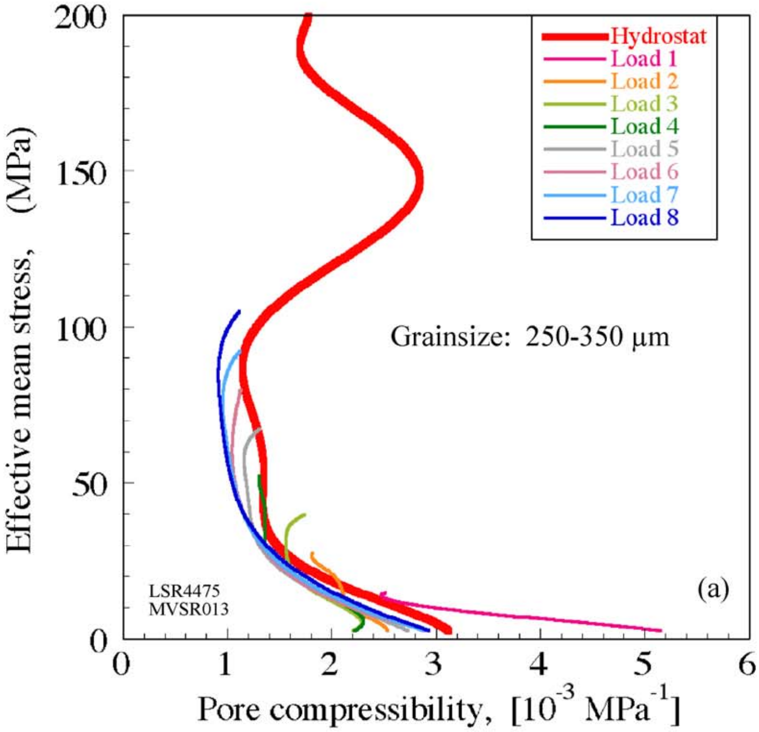
Hydrostat
Load 1
Load 2
Load 3
Load 4
Load 5
Load 6
Load 7
Load 8
Grainsize: 250-350 μm
LSR4475
MVSR013
(a)
Effective mean stress, (MPa)
Pore compressibility, [10^-3 MPa^-1]
0
50
100
150
200
0 1 2 3 4 5 6

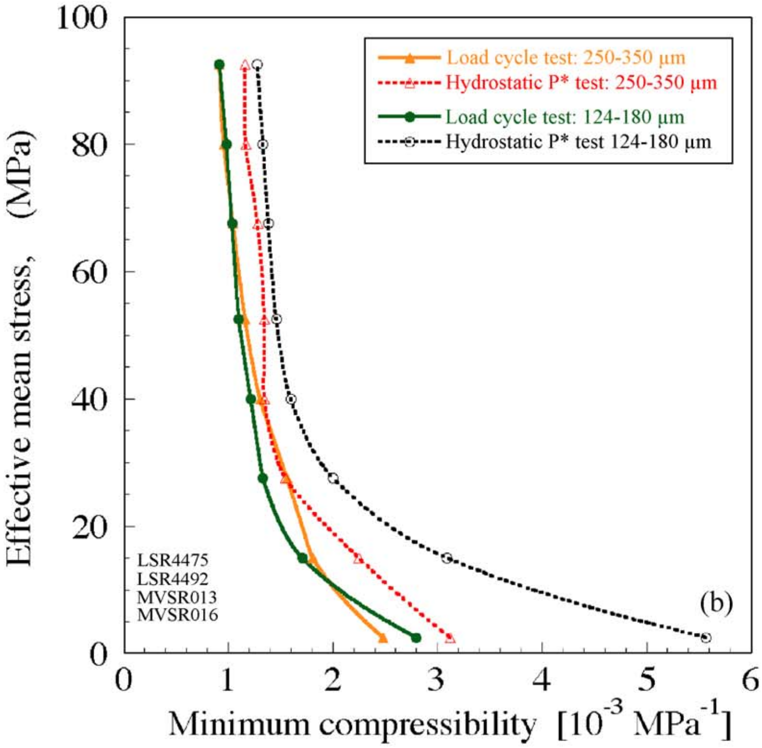
Load cycle test: 250-350 μm
Hydrostatic P* test: 250-350 μm
Load cycle test: 124-180 μm
Hydrostatic P* test 124-180 μm
LSR4475
LSR4492
MVSR013
MVSR016
(b)
Effective mean stress, (MPa)
Minimum compressibility [10^-3 MPa^-1]
0
20
40
60
80
100
0 1 2 3 4 5 6

stress rate test (Fig. 9b). This comparison indicates that pressure-dependent compaction (or improved consolidation) lowers the compressibility of granular sand. Furthermore, experiments on two different grain size fractions indicate that this observation is independent of particle dimension. Second, at stresses lower than the previous maximum effective pressure (PMMS) the compressibility curves generally overlie each other indicating good reproducibility for successive stress cycles (Fig. 9a). This implies that the material has the stiffness (hence, consolidation state) that was achieved during previous loadings. The third feature is observed for effective pressures that exceed the previous maximum pressure (PMMS). For these portions of a given stress cycle, pore compressibility increases slightly and approaches values of the hydrostatic constant stress rate test. This increase coincides with the secondary yielding that occurs when the reloading path meets the 'normal' consolidation curve. In this stage of the loading path, the sample exhibits a 'new' state of deformation in response to the new maximum applied pressure.

The low compressibilities for the portion of stress cycle reloads below the PMMS are associated with low AE rates (Fig. 5). We interpret this to indicate that the initial portion of stress cycle reloading reflects predominantly elastic deformation. The secondary yield and increased compressibility observed when the applied stress nears the PMMS must then reflect the onset of permanent strain. Thus, the 'normal' consolidation curve of our constant stress rate tests displays the combined effects of deformation involving elastic and permanent strain mechanisms.

4.4. Mathematical description of elastic deformation

To better understand elastic deformation of granular sand at stresses below P^*, we consider a Hertzian description of deformation between two contacting spherical bodies (Hertz, 1881; Timoshenko, 1934; Love, 1944; Mindlin and Deresiewicz, 1953; Gangi, 1978; Zhang et al., 1990a; Brzesowsky, 1995). This description begins with the assumption that a deforming granular aggregate is comprised of perfectly elastic, uniformly sized spheres subjected to external forces (Fig. 10). The spheres compress at their meeting point and the area of contact grows as a function of the applied force and material properties. From contact mechanics theory, the amount of closure between the sphere centres (α) and the radius of the circular contact (a) will change according to the following relations (after Gangi, 1978):

$$\alpha = 2R\left[\frac{3\pi KF}{4R^2}\right]^{2/3} \tag{2}$$

$$a = \left[\frac{3\pi KFR}{4}\right]^{1/3} \qquad \text{where } K = \frac{(1-\upsilon^2)}{\pi E} \tag{3}$$

Here, R is the grain radius, F is the applied force, K is the bulk modulus of the grain, υ and E are the Poisson ratio and Young's modulus, respectively, of the grain.

By expanding on Hertzian contact theory, Gangi, (1978) showed that pressure-dependent variations in whole rock transport properties can be calculated when granular compaction occurs through elastic deformation at grain contacts. Of relevance to our study are those relations used to determine porosity evolution with applied hydrostatic pressure:

$$\Phi(P) = \Phi_0\left[1 - C_0(P/P_{\mathrm{m}})^{2/3}\right]^3 \Big/ \left\{1 - \Phi_0 + \Phi_0\left[1 - C_0(P/P_{\mathrm{m}})^{2/3}\right]^3\right\} \tag{4}$$

$$P_{\mathrm{m}} = 4E/3\pi(1 - v^2) \tag{5}$$

where Φ is the porosity calculated for the applied pressure (P) such that $\Phi_0 = \Phi(0)$, C_0 is a "packing"

Fig. 9. Calculated pore compressibilities for our experiments according to Eq. (1), described in the text. (a) Compressibilities calculated for the constant stress rate and stress cycling tests (Figs. 2 and 5, respectively) are plotted against the applied effective pressure. After decreasing the applied stress, data for the reload cycles show that samples are less compressible than for the constant stress rate test. Lower compressibilities are interpreted to reflect greater consolidation of the granular aggregate. (b) Pore compressibilities calculated for hydrostatic experiments on samples with different particle size fractions. For the stress cycling tests, we show the minimum compressibility for a given loading curve as a function of the previous maximum mean stress (PMMS) that had been applied. These data show that the consolidation state is reproducible during deformation of the granular media.

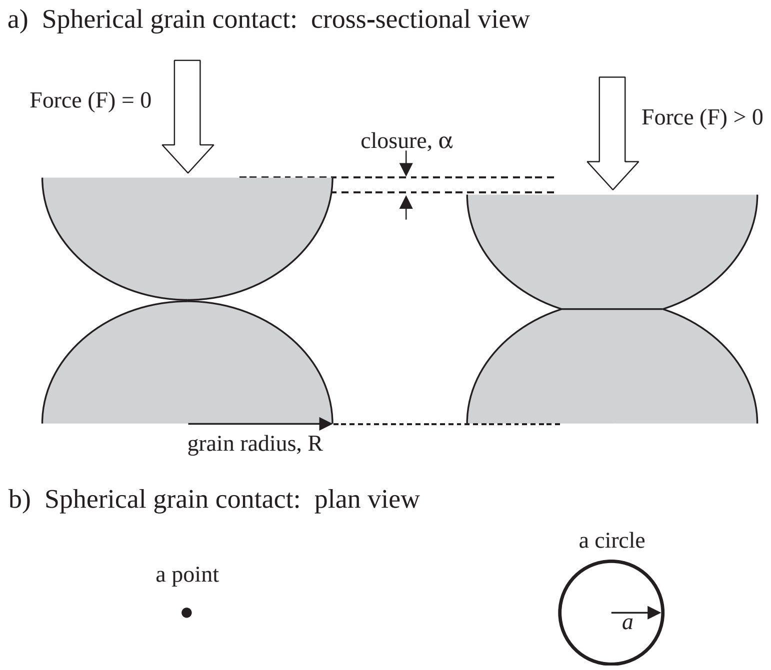

Fig. 10. Schematic diagram showing elastic distortion of two spherical grains in contact.

constant for the granular aggregate (of value ≈ 2), and P_m is the effective elastic modulus of the grains.

Using Eqs. (4) and (5), we calculate the evolution of porosity with applied hydrostatic pressure by assuming a typical starting porosity for our samples of $\sim 32\%$ and published material constants for α-quartz ($\upsilon = 0.099$, $E = 90.177$ GPa; after Birch, 1966; Sumino and Anderson, 1984). The predicted porosity evolution for hydrostatic loading is considerably less than our measurements of porosity reduction from hydrostatic constant stress rate tests (Fig. 11). Furthermore, the calculated porosity change is expected to be reversible unlike the non-recoverable strains observed from our stress cycling tests (Fig. 5). However, the Hertzian contact model predictions match closely the porosity data obtained from reloading portions of the hydrostatic stress cycle tests. When the numerical results are coupled with the low acoustic emission rates observed at reload stresses less than the PMMS, we may safely conclude that reload cycles represent the macroscopic response of the granular aggregate to elastic distortion at grain contacts.

4.5. Model for hydrostatic deformation

As we reasoned earlier, compaction within granular quartz sand at sub-critical pressures is achieved via a combination of Hertzian-style elastic deformation at grain contacts and inelastic strain mechanisms. These inelastic processes vary with effective mean stress and may include particle rolling, frictional sliding, grain rotation and rearrangement, and grain fracture. Based on the stresses and microseismicity measured during our deformation tests, we expect that grain fracture depends on both the level of macroscopic stress and the population density of particles in contact. On the other hand, grain rearrangement would depend on the directed macroscopic stresses that produce shear tractions and torques at grain contacts. While both processes operate for all stress states, grain rearrangement may be favoured at low mean pressures while grain fracture dominates at elevated stress conditions (either hydrostatic or triaxial).

The theoretical constraints of Hertzian behaviour for spherical grains are such that when pressure is below a critical level particles deform elastically, while above that stress particles yield by fracture or other modes of

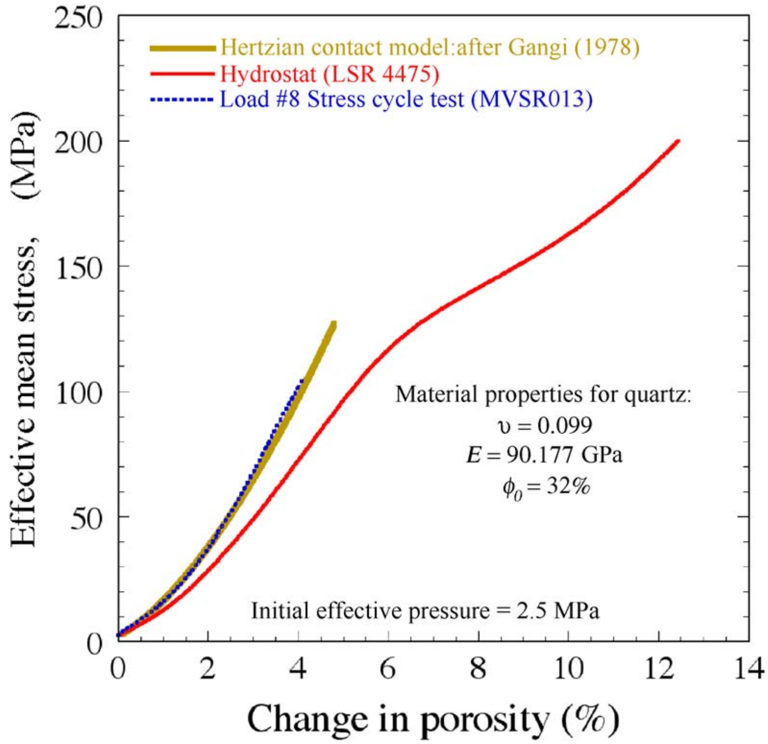

Fig. 11. Comparison of hydrostatic deformation tests to numerical calculations of compaction due to elastic deformation at grain contacts based on Hertzian contact theory. For the properties of our starting material, the elastic model predicts a stress–strain path that more closely matches reloading during a stress cycle test. This, combined with the low compressibilities observed from stress cycle tests, suggests that deformation during constant stress rate tests is accommodated through both elastic and inelastic strain mechanisms.

permanent deformation (Mindlin and Deresiewicz, 1953; Brzesowsky, 1995; Walker, 2000). Photoelastic studies and discrete element computer simulations indicate that the stresses applied to a granular aggregate are transmitted via a complicated network of stress bridges and force chains (e.g. Gallagher et al., 1974; Drescher and de Josselin de Jong, 1972; Morgan and Boettcher, 1999; Aharonov and Sparks, 1999). When the applied stress is sufficiently high, the population of grains at or near failure will be large. In turn, wholesale collapse of the stress bridges will occur and lead to macroscopically observed increases in volumetric strain rate.

We propose a three-component model that has been employed in studies of powder densification involving particle rearrangement, elastic deformation of grains, and grain failure (Reed, 1995; Walker, 2000; see Fig. 12). It is likely that these processes operate simultaneously during deformation of granular media, which makes it difficult to separate their contributions during the course of a laboratory experiment. However, these processes can be considered separately in conceptual models of granular deformation.

At low-effective pressures (e.g. <20 MPa in Fig. 3a), samples exhibit considerable inelastic volumetric strain but with comparatively little acoustic emission activity. Furthermore, direct observation of materials subjected to these pressures indicates only small amounts of fracturing and granulation (Fig. 4b). This indicates that the granular compaction that occurs early in the loading path does not result from brittle failure processes. Rather, it is likely that these large strains are achieved by acoustically silent processes such as granular rolling, particle rotation, and frictional slip at grain contacts (see Fig. 12a). This granular rearrangement acts to increase the population of grains that are in contact with their neighbours. As such, the granular aggregate achieves an

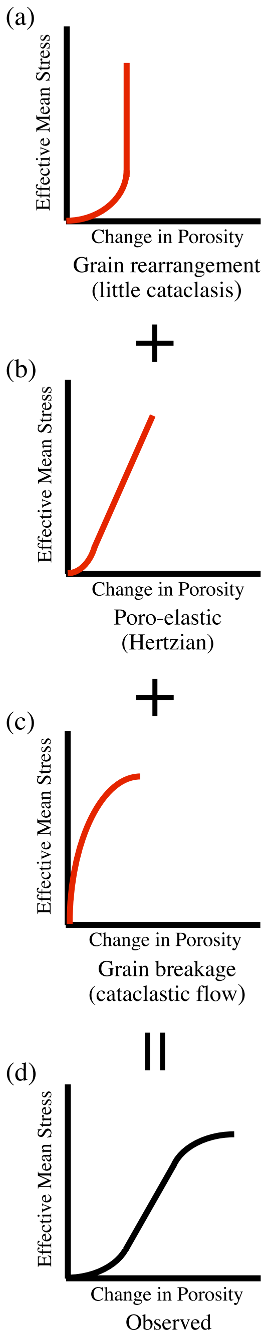

Fig. 12. Schematic model incorporating three simultaneously occurring deformation mechanisms that sum up to the stress–strain response observed during hydrostatic deformation tests.

optimal packing that is more capable of supporting the applied loads. As densification state improves due to continued granular rearrangement, volumetric strains will decrease as the applied stress becomes larger and deformation will have Hertzian-like elastic characteristics (see Fig. 12b). During this stage, fractures begin to be initiated as individual grains reach their failure limit with increased pressure.

With increased load, the aggregate continues to compact with an increased densification state that produces a less compressible material. Stresses supported at grain contacts and through stress bridges will increase and induce microcracking and failure of the grains (Fig. 4c). With greater applied stress, the population of grains near to failure will increase and result in higher AE rates. This eventually leads to the apparent macroscopic yield situation where significant grain cracking and failure occurs (Fig. 4d). As grain failure becomes more pervasive throughout the sample, stress bridges collapse and compactive strain rates accelerate considerably (Fig. 12c). This is consistent with observations of yielding behaviour of cohesive sandstones deformed at stresses that exceed a macroscopic crushing strength of the material (e.g. Zhang et al., 1990a,b; David et al., 1994; Wong et al., 1997; Baud et al., 2000). As such, the stress–strain character during this stage (Fig. 12c) is expected to mirror the functional form of the pressure dependence of microseismicity rates (Fig. 3b). Taken collectively, hydrostatic consolidation of granular media may be considered to result from the sum of non-brittle granular flow, elastic deformation at grain contacts, and granular cataclasis (Fig. 12d).

4.6. Model for triaxial compaction at elevated effective pressure

Samples subjected to elevated hydrostatic pressures exhibit significant volumetric compaction and reduced compressibility (Figs. 2, 3, 4, 5 and 9). The densification of these sand packs is expected to increase the population of contacting grains, as is indicated from the higher AE rates recorded at larger effective pressures. Yet when triaxial deformation is imposed at these elevated pressures, AE rates and volumetric strains increase significantly and samples exhibit lower ultimate strength compared to hydrostatic deformation at similar stress levels.

While both elastic and inelastic deformation processes operate during triaxial deformation at elevated effective pressure (e.g. Figs. 6 and 7), the increased AE rates suggest that grain failure is a favoured mechanism. Axial loading of samples would likely induce distortional stresses at particle contacts and promote grain failure. Furthermore, the population density of grain contacts would increase and favour the generation of stress bridges that have an optimal alignment relative to the imposed stress directions. For triaxial deformation, the force chain network would be strongly anisotropic. As individual particles reach their failure limit, the stress bridges would collapse and lead to macroscopic yielding of the sample at lower levels than for hydrostatic loading. With continued triaxial stressing, the rate of generation and collapse of these stress bridges would approach equilibrium. However, the evolutionary rates of these stress bridges are expected to be greater during triaxial deformation than for hydrostatic stressing, which would lead to larger volumetric strains.

5. Summary and implications

We have presented results from a suite of experiments designed to investigate mechanical deformation of unconsolidated granular media at elevated pressures. As the applied effective stress increases, quartz sand densifies and becomes less compressible with an associated increase in microcracking (as seen from optical micrographs and measured by elevated acoustic emission rates). Stress cycling experiments indicate that quartz sand exhibits permanent strains throughout the pressure range we studied. Large strains are recorded for low stresses, with a gradual transition to a quasi-linear stress-strain path at intermediate stresses. For high pressures, samples show a second transition to large strains associated with significant AE activity. This corresponds to macroscopic yield-like behaviour consistent with previous observations of a material crushing strength, P^* (e.g. Zhang et al., 1990a,b). Thus, inelastic strains are measured at low pressures well before acoustic emission (AE) rates are significant, and at higher pressures when large AE rates can be correlated with significant grain failure leading to an apparent critical failure point, P^*.

Analysis of our results leads to a physical model that describes the pressure-dependent compaction of an unconsolidated granular medium. At low pressures, quartz sand compacts predominantly via particulate flow involving grain rolling, slip at grain contacts, and grain translation. As the consolidation state increases with pressure, stresses build up at grain contacts and individual grains form stress bridges to support the macroscopic load. The formation and subsequent evolution of these stress bridges will be promoted by the distortional stresses imposed during triaxial deformation. At the grain scale, individual particles deform elastically following the Hertzian contact theory. Microcracks within the grains develop as stress builds up at grain contacts and with continued stressing these microcracks grow leading to grain failure. As the number of failing grains reaches a critical limit, the macroscopic stresses can no longer be supported and pore collapse occurs throughout the sample.

The observation that permanent strains accumulate at all pressures is fundamental for the definition of yielding of the granular aggregate. The classic definition of material yield relies on observations that pinpoint the onset of permanent deformation. As our sand exhibits permanent strain for all pressures, this implies that the aggregates are yielding at all stages of deformation. This observation is crucial for the construction of failure envelopes that are often reported in studies of critical state and CAP models of soil mechanics, and more recently extended to the loading conditions of rock mechanics (e.g. Wong et al., 1997; Karner et al., 2000). Our results indicate that the material crushing strength (e.g. P^* for hydrostatic deformation) must be carefully identified using a rigorous, self-consistent, and systematic approach.

Our stress cycling experiments also indicate that granular aggregates retain memory of the consolidation state that was previously attained. This is significant for studies of granular material in environments likely to experience fluctuations in stress due to deposition and erosion at an actively subsiding river delta; or within gouge zones of mature seismogenic faults. It is important to note that for our experiments we allowed fluid to escape during pore collapse. If the natural environment were to permit interstitial fluids to migrate away from the compacting aggregate, then the sediment would consolidate "normally". If, however, the fluids were prevented from migrating, consolidation of the granular aggregate would result in increased pressures for interstitial fluids. Conversely, underpressured fluids would result if the loading stresses were relieved because the sediment would retain a memory of the previous consolidation state. Thus, the consolidation state and physical properties of sediments will be sensitive to the history of loading and generation of overpressure in sedimentary basins. Similarly, the physical properties of granular fault gouges will be sensitive to the influence of the earthquake cycle on fluid-saturated seismogenic faults.

Acknowledgements

This research was supported by the Office of Basic Energy Sciences, Division of Chemical Sciences, Geosciences, and Biosciences, Department of Energy, under Grant No. DE-FG03-ER14887. We thank Tengfong Wong and an anonymous reviewer for their thorough and constructive comments and suggestions regarding this manuscript. The authors are extremely grateful to Andrew Hajash, Wenwu He, and Steven Lenz for their significant contributions to this work, and for the many stimulating discussions we have had with them. We express our utmost appreciation to Tony Gangi and Dave Sparks for their insightful comments and thoughts expressed about this research.

References

Aharonov, E., Sparks, D.W., 1999. Rigidity phase transitions in granular packing. Phys. Rev., E, 6890–6896.

Arbenz, J.K., 1989. The Ouachita system. In: Bally, A.W., Palmer, A.R. (Eds.), The Geology of North America, Volume A—An Overview. Geological Society of America, Boulder, CO, pp. 371–396.

Athy, L.F., 1930. Density, porosity, and compaction of sedimentary rocks. AAPG Bull. 65, 2433–2436.

Baud, P. Zhu, W., Wong, T.-F., 2000. Failure mode and weakening effect of water on sandstone. J. Geophys. Res. 105, 16371–16389.

Biot, M.A., 1941. General theory of three-dimensional consolidation. J. Appl. Phys. 12, 155–164.

Biot, M.A., 1973. Nonlinear and semilinear rheology of porous solids. J. Geophys. Res. 78, 4924–4937.

Birch, F., 1966. Compressibility; elastic constants. In: Clark Jr., S.P. (Ed.), Handbook of Physical Constants. Geol. Soc. Am. Mem., vol. 97, pp. 169–173.

Borg, I. Friedman, M. Handin, J., Higgs, D.V., 1960. Experimental deformation of St. Peter Sand: a study of cataclastic flow. In: Griggs, D., Handin, J. (Eds.), Rock Deformation. Geol. Soc. Am. Mem., vol. 79, pp. 133–191.

Brace, W.F., 1978. Volume changes during fracture and frictional sliding: a review. Pure Appl. Geophys. 116, 603–614.

Bridgwater, J., 1994. Mixing and segregation mechanisms in particle flow. In: Mehta, A. (Ed.), Granular Matter: An Interdisciplinary Approach. Springer, New York, pp. 161–193.

Britto, A.M., Gunn, M.J., 1987. Critical State Soil Mechanics via Finite Elements. Ellis Horwood, Chichester.

Brzesowsky, R.H., 1995. Micromechanics of Sand Grain Failure and Sand Compaction. PhD Thesis. Universiteit Utrecht, Netherlands.

Chester, J.S. Lenz, S.C. Chester, F.M., Lang, R., 2003. Mechanisms of compaction of quartz sand at diagenetic conditions. Earth Planet. Sci. Lett. (in press).

Chuhan, F.A. Kjeldstad, A. Bjørlykke, K., Høeg, K., 2002. Porosity loss in sand by grain crushing—experimental evidence and relevance to reservoir quality. Mar. Pet. Geol. 19, 39–53.

David, C. Wong, T.-F. Zhu, W., Zhang, J., 1994. Laboratory measurement of compaction-induced permeability change in porous rocks: implications for the generation and maintenance of pore pressure excess in the crust. Pure Appl. Geophys. 143, 425–456.

Dewers, T., Hajash, A., 1995. Rate laws for water-assisted compaction and stress-induced water–rock interaction in sandstones. J. Geophys. Res. 100, 13093–13112.

Drescher, A., de Josselin de Jong, G., 1972. Photoelastic verification of a mechanical model for the flow of a granular material. J. Mech. Phys. Solids 20, 337–351.

Elias, B.P., Hajash Jr., A., 1992. Changes in quartz solubility and porosity due to effective stress: an experimental investigation of pressure solution. Geology 20, 451–454.

Gallagher, J.J. Friedman, M. Handin, J., Sowers, G.M., 1974. Experimental studies relating to microfracture in sandstone. Tectonophysics 21, 203–247.

Gangi, A.F., 1978. Variation of whole and fractured porous rock permeability with confining pressure. Int. J. Rock Mech. Min. Sci. Geomech. Abstr. 15, 249–257.

Graham, J., Hovan, J.-M., 1986. Stress characteristics for bearing capacity in sand using a critical state model. Can. Geotech. J. 23, 195–202.

Graton, L.C., Fraser, H.J., 1935. Systematic packing of spheres—with particular relation to porosity and permeability. J. Geol. 43, 785–909.

Gudehus, G., 2000. On the physical background of soil strength. In: Kolymbas, D. (Ed.), Constitutive Modelling of Granular Materials. Springer, Berlin, pp. 291–301.

Handin, J. Friedman, M. Logan, J.M. Pattison, L.J., Swolfs, H.S., 1972. Experimental folding of rocks under confining pressure: buckling of single-layer rock beams. In: Heard, H.C., Borg, I.Y., Carter, N.L., Raleigh, C.B. (Eds.), Flow and Fracture of Rocks. AGU Geophys. Mono. Series, vol. 16, pp. 1–28.

He, W., 2001. Experimental and Theoretical Modeling of Creep

Compaction of Quartz Sand: rate Laws and Evolution of Porosity and Fluid Chemistry. PhD Dissertation. Texas A&M University. 90 pp.

Heard, H.C., 1963. Effect of large changes in strain rate in the experimental deformation of Yule marble. J. Geol. 71, 162–195.

Hedberg, H.D., 1926. The effect of gravitational compaction on the structure of sedimentary rocks. AAPG Bull. 10, 1035–1073.

Herle, I. Doanh, T., Wu, W., 2000. Comparison of hypoplastic and elastoplastic modelling of undrained triaxial tests on loose sand. In: Kolymbas, D. (Ed.), Constitutive Modelling of Granular Materials. Springer, Berlin, pp. 333–351.

Hertz, H., 1881. Ueber die Berührung fester elastischer Körper. J. Reine Angew. Math. 92, 156–171.

Karner, S.L. Chester, F.M. Kronenberg, A.K., Lenz, S.C., 2000. The compactive strength of granular quartz sand. EOS Trans. AGU 81 (48), F1187.

Karner, S.L., Chester, F.M., Kronenberg, A.K., Chester, J.S., Lenz, S.C., Hajash, A., He, W., 2001. Compressibility and particle size effects of compacted granular quartz. EOS Trans. AGU 82 (47), F1131

Karner, S.L. Chester, J.S. Chester, F.M. Kronenberg, A.K., Hajash, A., 2003. Laboratory deformation of granular quartz sand: implications for the burial of clastic rocks. AAPG Bull (submitted for publication).

Lenz, S.C., 2002. Acoustic Emission and Compaction Creep of Quartz Sand at Subcritical Stress. MSc Thesis. Texas A&M University, College Station, Texas.

Lord, A.E. Koerner, R.M., Curran, J.W., 1977. Fundamental studies of acoustic emissions in soils. In: Hardy, H.R., Leighton, F.W. (Eds.), Proceedings First Conference on Acoustic Emission/Microseismic Activity in Geologic Structures and Materials. Trans. Tech. Publications, Clausthal, Germany, pp. 135–148.

Love, A.E.H., 1944. A Treatise on the Mathematical Theory of Elasticity. Dover Publ., New York. 643 pp.

Marcher, Th. Vermeer, P.A., von Wolffersdorff, P.-A., 2000. Hypoplastic and elastoplastic modelling—a comparison with test data. In: Kolymbas, D. (Ed.), Constitutive Modelling of Granular Materials. Springer, Berlin, pp. 353–374.

Maxwell, J.C., 1964. Influence of depth, temperature, and geologic age on porosity of quartz sandstone. AAPG Bull. 48, 697–709.

Mindlin, R.D., Deresiewicz, H., 1953. Elastic spheres in contact under varying oblique forces. J. Appl. Math. 75, 327–344.

Morgan, J.K., Boettcher, M.S., 1999. Numerical simulations of granular shear zones using the distinct element method: 1. Shear zone kinematics and the micromechanics of localization. J. Geophys. Res. 104, 2703–2719.

Olgaard, D.L. Nueesch, R., Urai, J., 1995. Consolidation of water saturated shales at great depth under drained conditions. In: Fujii, T. (Ed.), Proceedings of the Congress of the International Society for Rock Mechanics, vol. 8, pp. 273–277.

Olgaard, D.L. Dugan, B.E., Gooch, M.J., 2001. Near-sea floor compaction and shallow overpressures: constraints from high strain consolidation tests on ODP sediments. EOS Trans. AGU 82 (47), F1128.

Pitman, J.K. Goldhaber, M.B., Spöetl, C., 1997. Regional diagenetic patterns in the St. Peter sandstone: implications for brine migration in the Illinois basin. U.S. Geol. Surv. Bull. 2094-A, A1–A17.

Ramsamooj, D.V., Alwash, A.J., 1990. Model prediction of cyclic response of soils. J. Geotech. Eng. 116, 1053–1072.

Reed, J.S., 1995. Principles of Ceramic Processing, 2nd ed. Wiley, New York.

Schofield, A., Wroth, P., 1968. Critical State Soil Mechanics. McGraw-Hill, New York. 310 pp.

Smith, P.R. Jardine, R.J., Hight, D.W., 1992. The yielding of Bothkenar clay. Géotechnique 42, 257–274.

Sumino, Y., Anderson, O.L., 1984. Elastic constants of minerals. In: Carmichael, R.S. (Ed.), CRC Handbook of Physical Properties of Rocks, vol. III. CRC Press, Boca Raton, pp. 92–93.

Terzaghi, C., 1925. Principles of soil mechanics: II. Compressive strength of clay. Eng. News-Rec. 95, 796–800.

Timoshenko, S., 1934. Theory of Elasticity. McGraw-Hill, New York.

Walker Jr., W.J., 2000. Persistence of granular structure during die compaction of ceramic powders. Mater. Res. Soc. Symp. Proc. 627 (BB6.4).

Wong, T.-F. David, C., Zhu, W., 1997. The transition from brittle faulting to cataclastic flow in porous sandstones: mechanical deformation. J. Geophys. Res. 102, 3009–3025.

Zhang, J. Wong, T.-F., Davis, D.M., 1990a. Micromechanics of pressure-induced grain crushing in porous rocks. J. Geophys. Res. 95, 341–352.

Zhang, J. Wong, T.-F. Yanagidani, T., Davis, D.M., 1990b. Pressure-induced microcracking and grain crushing in Berea and Boise sandstones: acoustic emission and quantitative microscopy measurements. Mech. Mater. 9, 1–15.

Zimmerman, R.W., 1991. Compressibility of Sandstones. Elsevier, New York. 173 pp.

Zoback, M.D., Byerlee, J.D., 1976. Effect of high-pressure deformation on permeability of Ottawa sand. AAPG Bull. 60, 1531–1542.